



Measurements on ATP induced cellular fluctuations using real-time dual view transport of intensity phase microscopy

YANKE SHAN,^{1,5} QINGTAO GONG,^{1,2,5} JIAN WANG,¹ JING XU,^{1,2} QI WEI,^{1,2} CHENG LIU,^{2,3} LIANG XUE,⁴ SHOUYU WANG,^{1,2,6} AND FEI LIU^{1,7}

¹Joint International Research Laboratory of Animal Health and Food Safety of Ministry of Education & Single Molecule Nanometry Laboratory (Sinmolab), Nanjing Agricultural University, Nanjing, Jiangsu 210095, China

²Computational Optics Laboratory, School of Science, Jiangnan University, Wuxi, Jiangsu 214122, China

³Shanghai Institute of Optics and Fine Mechanics, Chinese Academy of Sciences, Shanghai 201800, China

⁴College of Electronics and Information Engineering, Shanghai University of Electric Power, Shanghai 200090, China

⁵These authors contributed equally to this work.

⁶shouyu@jiangnan.edu.cn

⁷feiliu24@njau.edu.cn

Abstract: Dual view transport of intensity phase microscopy is adopted to quantitatively study the regulation of adenosine triphosphate (ATP) on cellular mechanics. It extracts cell phases in real time from simultaneously captured under- and over-focus images. By computing the root-mean-square phase and correlation time, it is found that the cellular fluctuation amplitude and speed increased with ATP compared to those with ATP depletion. Besides, when adenylyl-imidodiphosphate (AMP-PNP) was introduced, it competed with ATP to bind to the ATP binding site, and the cellular fluctuation amplitude and speed decreased. The results prove that ATP is a factor in the regulation of cellular mechanics. To our best knowledge, it is the first time that the dual view transport of intensity phase microscopy was used for live cell phase imaging and analysis. Our work not only provides direct measurements on cellular fluctuations to study ATP regulation on cellular mechanics, but it also proves that our proposed dual view transport of intensity phase microscopy can be well used, especially in quantitative phase imaging of live cells in biological and medical applications.

© 2019 Optical Society of America under the terms of the [OSA Open Access Publishing Agreement](#)

1. Introduction

It is known that cells constantly sense and adapt to their biochemical environments by adjusting its mechanical properties [1] which play an important role in cell spreading [2], cell adhesion [3], motility [4,5] and proliferation rates [6], as well as more fundamental biological processes, such as the lineage specification of stem cells, control of cell growth and apoptosis [7,8]. Mechanical properties of cells are metabolically regulated to control the static and dynamic cellular characteristics. Not only intracellular but also extracellular ATP can affect cell proliferation, migration, differentiation, contraction and relaxation, wound healing, inflammation and cancer [2]. The process of chemosensing of extracellular ATP by cells involves a multistep cascade [9,10] that results in information exchange through physically contacting cells or through diffusing signaling molecules [11]. One important mechanical element of the cell affected by ATP is its plasma membrane, a dynamic fluid lipid bilayer that is not static but actively regulated. For example, it has been shown that ATP is crucial in maintaining the biconcave shape of the red blood cell membrane [12], and can increase the

dynamic membrane fluctuations of red blood cells [13,14]. However, the regulatory mechanism of ATP in cell membranes is mainly investigated for red blood cells [15,16], how ATP regulates mechanical properties of the cell membrane of other cell types still remains elusive.

Cellular fluctuation which is often induced by cellular membrane vibration can quantify the mechanics of live cells. To obtain the direct measurements on the cellular fluctuations of live cells, different methods have been proposed including the point dark field microscopy [12], the reflection interference contrast microscopy [13] and the optical tweezer based interferometric method [14], etc. Compared to these conventional techniques, quantitative phase microscopy [17–21] is a better choice. This technique not only obtains high-contrast images of label-free samples, but also provides cellular parameters in details; therefore, it is especially suits for cellular fluctuation measurements. There are many quantitative phase microscopic methods based on different principles but all focusing on sample phase extraction. Ptychography based techniques including ptychographic iterative engine [22–24] and Fourier ptychographic microscopy [25–27] can provide cell phases with high accuracy and resolution. However, due to the indispensable time-consuming iteration, ptychography can hardly be used for real-time live cell imaging. Interferometry based techniques such as digital holographic microscopy [28–32] and quantitative interferometric microscopy [33–40] can extract cell phases even from single-shot fringe pattern, indicating its real-time quantitative phase imaging capability. While reference beam and coherent illumination are required, it is difficult to integrate the interferometry with the widely used commercial microscopes. Besides these methods, transport of intensity phase microscopy [41–45] is a potential tool for live cell imaging and analysis, because it can be easily integrated with commercial microscopes only with simple modification, and the sample phases can be retrieved rapidly without time-consuming iteration or phase unwrapping. Though multi-focal intensities are required, different methods were proposed to capture the multi-focal intensities simultaneously. Relying on the chromatic aberration, Waller group designed the single-shot color transport of intensity phase microscopy [46], while it ignores the sample dispersion. Besides, based on the field of view (FoV) division, Waller et al. [47], Yang et al. [48] and Yu et al. [49] proposed single-shot transport of intensity phase microscopy using volume holography, grating and spatial light modulator, respectively. Li et al. [50] and Zuo et al. [51] also designed mirror-prism based single-shot transport of intensity phase microscopy. Using these methods, multi-focal intensities can be simultaneously collected at a single imaging plane. Unfortunately, the imaging FoVs of these methods are obviously limited, and these systems are often complicated. In order to simplify the system, as well as to maintain the large FoV, we have proposed dual view transport of intensity phase microscopy [52]. First, both under- and over-focus images can be simultaneously captured by setting two identical image recorders on the binocular of the commercial microscope. Then after FoV correction on these simultaneously captured multi-focal images and in-focus plane determination [53], the in-focus image can be approximated to the average of under- and over-focus images [54,55]. Finally, the phase can be extracted from multi-focal images by solving the Poisson equation. Compared to the classical ptychography and interferometry, dual view transport of intensity phase microscopy not only has fast processing speed skipping time-consuming iteration and phase unwrapping, but also can be easily integrated with commercial microscopes, more importantly, it can realize real-time cell phase measurements for cellular fluctuation detection. Therefore, in this paper, we used the dual view transport of intensity phase microscopy to detect the cellular fluctuations. Cellular fluctuations of both F81 and BHK21 cells with ATP and with ATP depletion as well as by introducing adenylyl-imidodiphosphate (AMP-PNP) were measured in order to study the function of ATP on cellular mechanics. Moreover, both the root-mean-square phase and the correlation time were computed to analyze cellular fluctuation amplitude and speed, respectively. It is found that cellular fluctuation amplitude and speed increased with ATP compared to those with ATP

depletion. Besides, when AMP-PNP was introduced which competed with ATP to bind to the ATP binding site, the cellular fluctuation amplitude and speed decreased. The results prove that ATP is a factor to regulate cellular mechanics. To our best knowledge, it is the first time that the dual view transport of intensity phase microscopy is successfully used for live cell phase imaging and analysis, and it is believed the work not only provides a reference for understanding the ATP function on cellular fluctuations, but also proposes a tool for measuring cellular dynamics in real time.

2. Real-time cell phase imaging and cellular fluctuation analysis method

2.1 Real-time cell phase imaging using dual view transport of intensity phase microscopy

The dual view transport of intensity phase microscopy was adopted for real-time cell phase measurements. Since high coherence of the illumination is required for accurate phase retrieval in transport of intensity phase microscopy, an interference filter (Daheng Optics, China) with the central wavelength of 633 nm and the full width at half maximum of 10 nm was inserted into the light source system for high temporal coherence; besides, the condenser aperture of the Kohler illumination was set as $\sim 40\%$ of the objective aperture for high spatial coherence. Two identical CMOS cameras (JAI, Japan) were set at the binocular of a commercial microscope (Eclipse Ti, Nikon, Japan), and their focal planes were set at different planes with the interval of 3 mm by brass spacer rings (Edmund Optics, US) as shown in Fig. 1(A). Unfortunately, there was inevitable FoV mismatch between these simultaneously captured multi-focal images in Fig. 1(B), which could hardly be corrected by manually adjusting CMOS cameras. In order to solve the problem, we designed the phase correlation based digital FoV correction method [53] to recognize and compensate the FoV mismatch. Via computing the cross power spectrum in frequency domain, the rotation, scale and translation between the simultaneously captured multi-focal images can be accurately determined; and even two images are not captured in the same focal plane, the adopted phase correlation based digital FoV correction method can still provide high-accurate FoV correction. The phase correlation based digital FoV correction method was both proved by numerical simulations and practical experiments in our previous work [53]. Additionally, in our experiments, 3-mm brass spacer rings were used to simultaneously obtain the multi-focal images, therefore, the focal distance between the simultaneously captured multi-focal images was 3 mm . Next, by adjusting the micro-objective of the inverted microscope, different multi-focal images can be captured. With the phase correlation based digital FoV correction method, the captured multi-focal images can be corrected with the same FoV. It is known that the image in the central place of these two imaging planes can be approximated to the average of the corrected multi-focal images. By adjusting the micro-objective, a series of multi-focal images as well as the computed central images were obtained. By evaluating these computed central images using in-focus criteria, the in-focus central image was determined, and the micro-objective was set at the corresponding position. In this condition, the captured images are the under- and over-focus images with the focal distance of 3 mm as indicated in Fig. 1(C). After FoV correction and under- and over-focus image determination, the in-focus image in Fig. 1(D) could be approximated to the average of the FoV corrected under- and over-focus intensities, as $I_{in} = (I_{under} + I_{over})/2$, in which I_{under} , I_{in} and I_{over} indicate the under-, in- and over-focus intensities, respectively. Then the quantitative phase distribution φ in Fig. 1(D) was retrieved by solving the Poisson equation using the fast Fourier transform (FFT) based phase retrieval method.

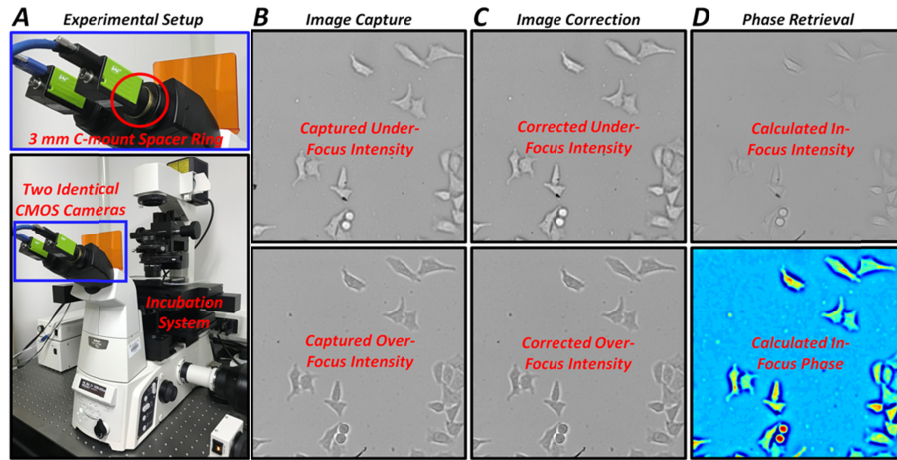


Fig. 1. Flowchart of the dual view transport of intensity phase microscopy. (A) the dual view transport of intensity phase microscopy system; (B) simultaneously recorded under- and over-focus images; (C) FoV corrected under- and over-focus images; (D) retrieved in-focus intensity and phase.

2.2 Cellular fluctuation analysis based on root-mean-square phase and correlation time computation

It is known that cell phase distribution which is proportional to the cell optical thickness can reflect the cellular fluctuations, therefore in order to measure the cellular fluctuations, here root-mean-square phase and correlation time were used to quantitatively describe the fluctuation amplitude and speed, respectively. Equation (1) reveals the definition of the root-mean-square phase, showing that higher root-mean-square phase ϕ_{rms} indicates increased cellular fluctuation amplitude. In Eq. (1), \mathbf{r} indicates the Cartesian coordinates, t_i means the corresponding time of the sampling phase, n is the total sampling number (number of the captured images in an observation period), and $N[\phi(\mathbf{r})]$ is the mean value of $\phi(\mathbf{r})$.

$$\phi_{rms}(\mathbf{r}) = \sqrt{\frac{1}{n-1} \sum_{i=1}^n \{\phi(\mathbf{r}, t_i) - N[\phi(\mathbf{r})]\}^2} \quad (1)$$

Besides, Eq. (2) lists the phase correlation function ρ , which statistically analyzes the fluctuation speed [56] and is similar to the phase correlation imaging [57]. The phase correlation coefficient reflects the correlation between the phases at time t ($\phi(t)$) and at time $t + \Delta t$ ($\phi(t + \Delta t)$). In Eq. (2), $\langle \rangle$ indicates the correlation computation. When $\Delta t = 0$, the phase correlation value equals 1; otherwise when Δt becomes larger, the phase correlation value decreases. The correlation time is defined as ΔT when the phase correlation value decreases to $1/e$ as shown in Eq. (3). According to the definition of the correlation time, when its value is small, it indicates a rather fast cellular fluctuation speed; otherwise when its value is large, cells perform slow fluctuation speed.

$$\rho(\Delta t) = \frac{\langle \phi(t), \phi(t + \Delta t) \rangle}{\delta^2} \quad (2)$$

$$\Delta T = \Delta t \Big|_{\rho(\Delta t)=1/e} \quad (3)$$

Figure 2 shows the flowchart of the cellular fluctuation analysis. First, following the procedures of the dual view transport of intensity phase microscopy, real-time phases of the a fixed FoV are obtained as shown in Fig. 2(A). Then, cells can be recognized according to the phase values as shown in Fig. 2(B), in which m indicates the pixel number of a single recognized cell. Next, for a single recognized cell, both the root-mean-square phase and the

correlation time within the recognized cell range can be extracted from the real-time phase distributions as shown in Fig. 2(C). Finally, the average values of the root-mean-square phase and the correlation time of a single cell are computed to characterize the cellular fluctuations, and the cellular fluctuations of multiple cells are also characterized as shown in Fig. 2(D) in order to statistically analyze the ATP induced cellular fluctuations.

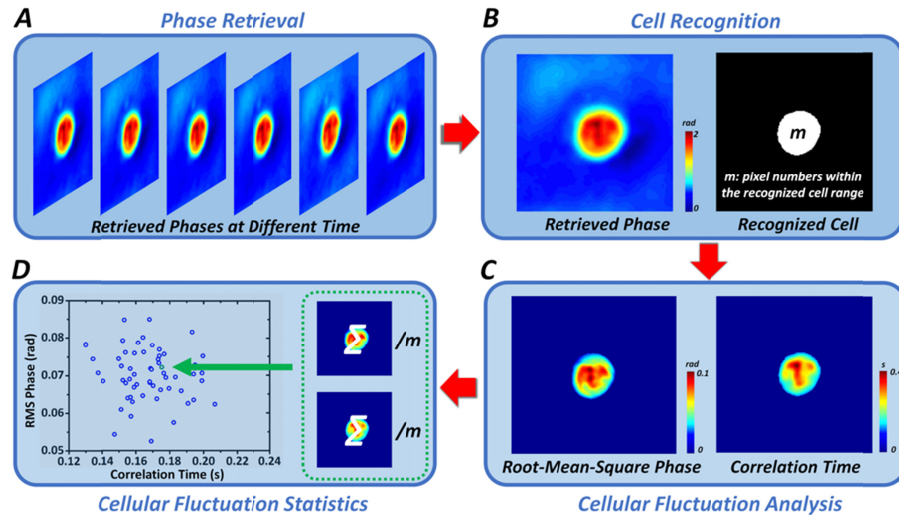


Fig. 2. Flowchart of cellular fluctuation analysis. (A) retrieved real-time phase distributions using dual view transport of intensity phase microscopy; (B) cell recognition according to the phase value; (C) the root-mean-square phase and the correlation time of a single cell; (D) statistical analysis on average root-mean-square phase and correlation time of multiple cells.

With the dual view transport of intensity phase microscopy and the cellular fluctuation analysis, it is possible to study the ATP induced cellular fluctuations. In the following section, cellular fluctuations of two kinds of cells were measured and analyzed in different conditions with ATP and with ATP depletion as well as by introducing AMP-PNP in order to study the ATP induced cellular fluctuations.

3. Cellular fluctuation measurements and analysis

3.1 Quantitative certification on the dual view transport of intensity phase microscopic system

Before cellular fluctuation measurements and analysis, a random phase plate (fabricated by Shanghai Institute of Optics and Fine Mechanics, Chinese Academy of Sciences) as a standard sample was first measured to certify the accuracy of the dual view transport of intensity phase microscopic system. There are only two phase steps in the random phase plate with the phase difference of π at the illumination of 633 nm . Figures 3(A) and 3(B) are the under- and over-focus images after FoV correction. Figure 3(C) is the extracted phase according to the FFT based phase retrieval algorithm, and the result obviously shows that there was a phase step with the phase difference of $\sim\pi$ under the illumination of 633 nm , and it is also illustrated with the cross section phase distributions shown in Fig. 3(D). It is known that the transport of intensity phase microscopy only provides the second order derivative of the phase, thus often misses low-frequencies and introduces errors in the phase reconstruction. Though more multi-focal images can effectively increase the phase reconstruction accuracy [58–62], massive image recording inevitably limits the real-time imaging capability. According to the experimental certification using the random phase plate, it is still proved that the dual view transport of intensity phase microscopy is able to retrieve phase in high accuracy even only two under- and over-focus images are recorded. Therefore,

the dual view transport of intensity phase microscopy was used here for real-time phase measurements for further cellular fluctuation analysis.

Moreover, in order to test the stability of the system, the real-time phase distributions of the same random phase plate in 6 s with the acquisition rate of 20 *fps* were obtained using dual view transport of intensity phase microscopy. Figures 3(E) and 3(F) show part of the under- and over-focus images as well as the retrieved phase distributions. In order to quantitatively characterize the phase noise, Fig. 3(G) shows the phase distributions of 3 sampling points on the random phase plate shown in Fig. 3(C) during the observation period. The extremely low root-mean-square phases (which are much lower than those of fluctuated live cells) prove that the dual view transport of intensity phase microscopic system was stable during the observation period.

According to the quantitative certification on both phase retrieval accuracy and stability, it is believed that the dual view transport of intensity phase microscopic system could provide cell phases in high accuracy and good stability. It was next adopted in the live cell phase measurements and cellular fluctuation analysis.

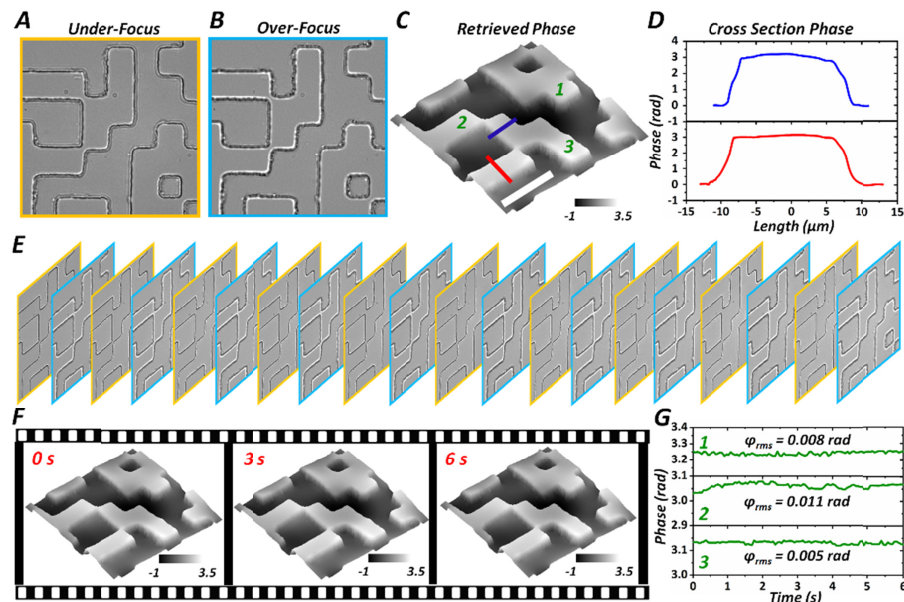


Fig. 3. Quantitative certification on the dual view transport of intensity phase microscopic system using random phase plate. (A) and (B) simultaneously recorded under- and over-focus images after digital FoV correction; (C) retrieved phase from (A) and (B); (D) cross section phase distributions along the lines in (C); (E) part of under- and over-focus images in an observation period of 6 s with the acquisition rate of 20 *fps*; (F) retrieved phase distributions at 0 s, 3 s and 6 s; (G) phase distributions of 3 sampling points on the random phase plate in (C) during the observation period. The color bars in (C) and (F) indicate the phase with the unit of rad, and the white bar in (C) indicates 30 μm .

3.2 Cellular fluctuation measurements and analysis with ATP and with ATP depletion

F81 and BHK21 cells were cultured in the DMEM supplemented with 10% fetal bovine serum (FBS, Gibco, US) at 37 °C in an atmosphere of humidified 5% CO₂. The cells were plated on the 35-mm plastic-bottom Petri dish (Thermo Fisher, US) for 24 h before experiments. In order to quantitatively measure and analyze the cellular fluctuations with ATP and with ATP depletion, both cell phase distributions were measured in the DMEM with and without glucose.

Before cellular measurements, a control experiment was first implemented to check the precision of the cellular fluctuation statistics. Both F81 and BHK21 cells were cultured in the

DMEM with glucose as well as the DMEM without glucose. With the certificated dual view transport of intensity phase microscopic system, these cell phases were retrieved during the observation period of 6 s with the acquisition rate of 20 fps. It is known that the cell can be recognized according to the retrieved phase in Fig. 2, therefore the cell occupied pixels were determined according to Fig. 4(A). We compared the cell occupied pixels during the period of 6 s from totally 40 cells (10 cells in each condition) as shown in Fig. 4(B), the changed pixel numbers were always less than 5% of the total cell occupied pixel numbers in all conditions. Since the cell random movements during the observation time were not obvious in our experiments, the cell movements were not considered in the following measurements.

Moreover, the dynamic phases of different F81 and BHK21 cells cultured in the same condition but in different times were also checked. Phase dynamics during 6 s of totally 12 cells were measured in two times with the interval of ~ 5 min, and their relative root-mean-square phase changes and correlation time changes were listed in Fig. 4(C). According to the rather low relative changes listed in Fig. 4(C), there were no statistically significant differences between the root-mean-square phase and the correlation time in two different periods, indicating that the cellular fluctuations of these two kinds of cells were stable.

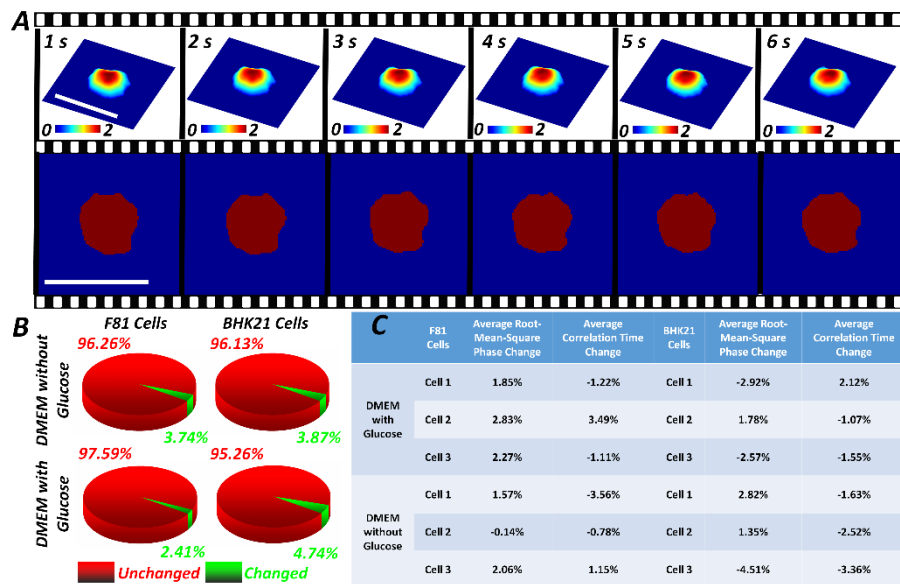


Fig. 4. Quantitative certification on the dual view transport of intensity phase microscopic system using cells. (A) cell phases and corresponding cell occupied pixels during the observation time; (B) statistical cell occupied pixel changes in different conditions; (C) relative root-mean-square phase changes and correlation time changes in different conditions. The color bars in (A) indicate the phase with the unit of rad, and the white bar in (A) indicates 30 μm .

After the above certifications, F81 cells were first cultured in the DMEM with high glucose (Gibco, US), so that enough ATP could be generated. The observation period and the acquisition rate still kept as 6 s and 20 fps, respectively. Figures 5(A) and 6(A) list the retrieved phases of representative 4 of the total 120 cells. The phase dynamics in this observation period reflect the cellular fluctuations with ATP. Next, the DMEM with high glucose was replaced by the DMEM without glucose (Gibco, US), and more than half of the ATP in the cells was depleted after 10 min [63]. After 10 min of the DMEM replacement, the under- and over-focus intensities were simultaneously recorded to recover the real-time phase distributions still for the same FoV, and the retrieved phase distributions of these 4 cells are still listed in Figs. 5(B) and 6(B). The observation time and the acquisition rate were the same as before, and the phase dynamics in this observation period represent the cellular fluctuations

with ATP depletion. Finally, ATP (Sigma-Aldrich, US) and glucose (Sinopharm, China) were added in the DMEM without glucose, respectively. After 10 min of ATP or glucose adding, the under- and over-focus intensities were simultaneously recorded to recover the real-time phase distributions as shown in Figs. 5(C) and 6(C). The only difference between Figs. 5 and 6 is that in Fig. 5, ATP was added; while in Fig. 6, glucose was added in the final step. The phase dynamics in this observation period indicate the cellular fluctuations with ATP. Though Figs. 5/6(A)-5/6(C) only list 4 representative cells, in order to statistically evaluate the cellular fluctuations, total 60 F81 cells were measured with the experimental condition in Fig. 5; and another 60 cells were measured with the experimental condition in Fig. 6. Additionally, to quantitatively and statistically evaluate the cellular fluctuations, average root-mean-square phase and correlation time of all the measured cells were computed in Figs. 5/6(D), 5/6(E) and 5/6(F) corresponding to the conditions in Figs. 5/6(A), 5/6(B) and 5/6(C). The statistical root-mean-square phase and correlation time were calculated as 0.0690 ± 0.0075 rad, 0.1607 ± 0.0227 s/ 0.0705 ± 0.0074 rad, 0.1585 ± 0.0217 s; 0.0615 ± 0.0066 rad, 0.1780 ± 0.0141 s/ 0.0617 ± 0.0066 rad, 0.1821 ± 0.0193 s; and 0.0702 ± 0.0067 rad, 0.1688 ± 0.0175 s/ 0.0678 ± 0.0070 rad, 0.1686 ± 0.0159 s in Figs. 5/6(D), 5/6(E) and 5/6(F), respectively. Figures 5/6(G) show the statistical comparisons on both the root-mean-square phase and the correlation time. According to Student's t test, there are no statistically significant differences between the root-mean-square phase and the correlation time in Figs. 5/6(D) and 5/6(F), indicating that cellular fluctuations in these conditions are close both reflecting the conditions with ATP. While there are statistically significant differences between the root-mean-square phase and the correlation time in Figs. 5/6(E) and 5/6(D/F) ($t < 0.01$). The statistical root-mean-square phase with ATP is obviously higher than that with ATP depletion, and the statistical correlation time with ATP is also obviously lower than that with ATP depletion, indicating that cells performed increased fluctuation amplitude and speed with ATP than with ATP depletion. Additionally, linear discriminant analysis was also adopted for analyzing the cell fluctuations with and without ATP. With linear discriminant analysis, the two classes are as far apart as possible after classification, and the samples in the same class are as aggregated as possible [64]. Figures 5/6(G) show the classification results, when the cells were cultured with ATP, most of them were distributed upon the classification line, while when the cells were cultured without ATP, most of them were distributed below the classification line.

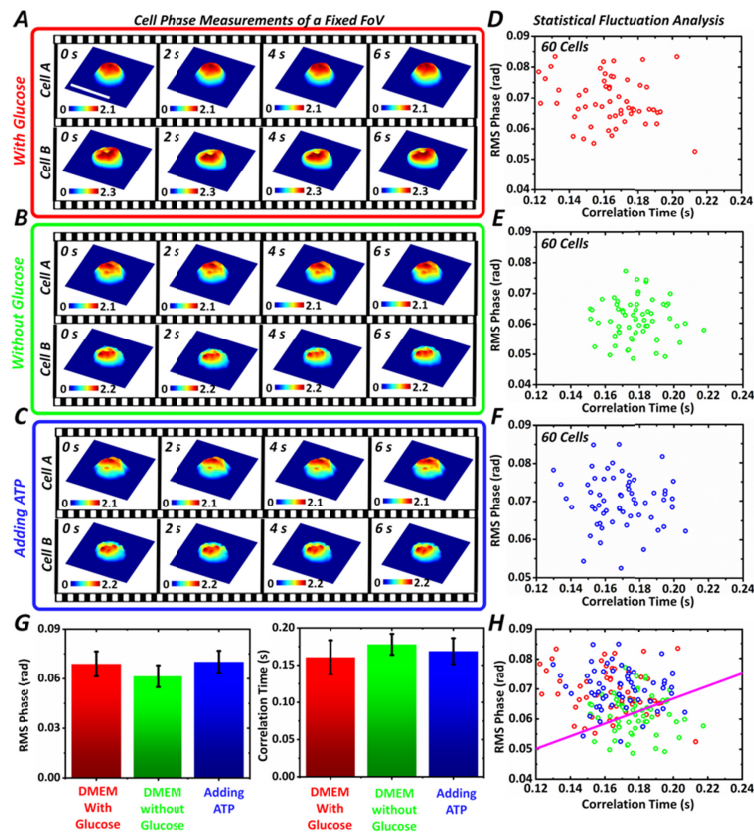


Fig. 5. Cellular fluctuations of F81 cells with ATP and with ATP depletion. (A), (B) and (C) the retrieved phases of 2 representative cells in the DMEM with glucose, in the DMEM without glucose and with ATP adding, respectively. (D), (E) and (F) statistical analysis on the average root-mean-square phase and the correlation time of 60 cells in different conditions corresponding to (A), (B) and (C). (H) Comparisons on the statistical root-mean-square phase and correlation time in different conditions. There are statistically significant differences between the root-mean-square phase and the correlation time in (E) and (D/F) ($t < 0.01$), but there are no statistically significant differences between the root-mean-square phase and the correlation time in (D) and (F). (G) Cell condition classification using linear discriminant analysis. The color bars in (A)-(C) indicate the phase with the unit of rad, and the white bar in (A) indicates $30 \mu\text{m}$. The error bars in (H) indicates the standard deviation.

Additionally, as another example, cellular fluctuations of BHK21 cells were also measured using dual view transport of intensity phase microscopy as shown in Figs. 7 and 8. Same to the measurements on F81 cells, the retrieved phases corresponding to 4 representative cells of total 120 cells in Figs. 7(A) and 8(A) show the case when BHK21 cells were cultured in the DMEM with high glucose; those in Figs. 7(B) and 8(B) reflect the condition when the DMEM with glucose was replaced by the DMEM without glucose; and those in Figs. 7(C) and 8(C) reveal the case when ATP and glucose were respectively introduced in the DMEM without glucose. The only difference between Figs. 7 and 8 is that in Fig. 7, ATP was added; while in Fig. 8, glucose was added in the final step. The statistical root-mean-square phase and correlation time were calculated as $0.0676 \pm 0.0077 \text{ rad}$, $0.1690 \pm 0.0203 \text{ s}$ / $0.0695 \pm 0.0058 \text{ rad}$, $0.1630 \pm 0.0148 \text{ s}$; $0.0587 \pm 0.0061 \text{ rad}$, $0.1826 \pm 0.0207 \text{ s}$ / $0.0581 \pm 0.0064 \text{ rad}$, $0.1819 \pm 0.0218 \text{ s}$; and $0.0674 \pm 0.0066 \text{ rad}$, $0.1689 \pm 0.0177 \text{ s}$ / $0.0691 \pm 0.0065 \text{ rad}$, $0.1639 \pm 0.0168 \text{ s}$ from totally 120 BHK21 cells in Figs. 7/8(D), 7/8(E) and 7/8(F), respectively. Figures 7/8(G) show the statistical comparisons on both the root-mean-square phase and the correlation time. According to Student's t test, there are no statistically

significant differences between the root-mean-square phase and the correlation time in Figs. 7/8(D) and 7/8(F), indicating that cellular fluctuations in these conditions are close both reflecting the conditions with ATP. While there are statistically significant differences between the root-mean-square phase and the correlation time in Figs. 7/8(E) and 7/8(D/F) ($t < 0.01$). The statistical root-mean-square phase with ATP is obviously higher than that with ATP depletion, and the statistical correlation time with ATP is obviously lower than that with ATP depletion, indicating that the BHK21 cells performed increased fluctuation amplitude and speed with ATP than with ATP depletion, which are similar to the results of the F81 cells. Additionally, linear discriminant analysis was also adopted for analyzing the cell fluctuations with and without ATP. Figures 7/8(G) show the classification results, when the cells were cultured with ATP, most of them were distributed upon the classification line, while when the cells were cultured without ATP, most of them were distributed below the classification line.

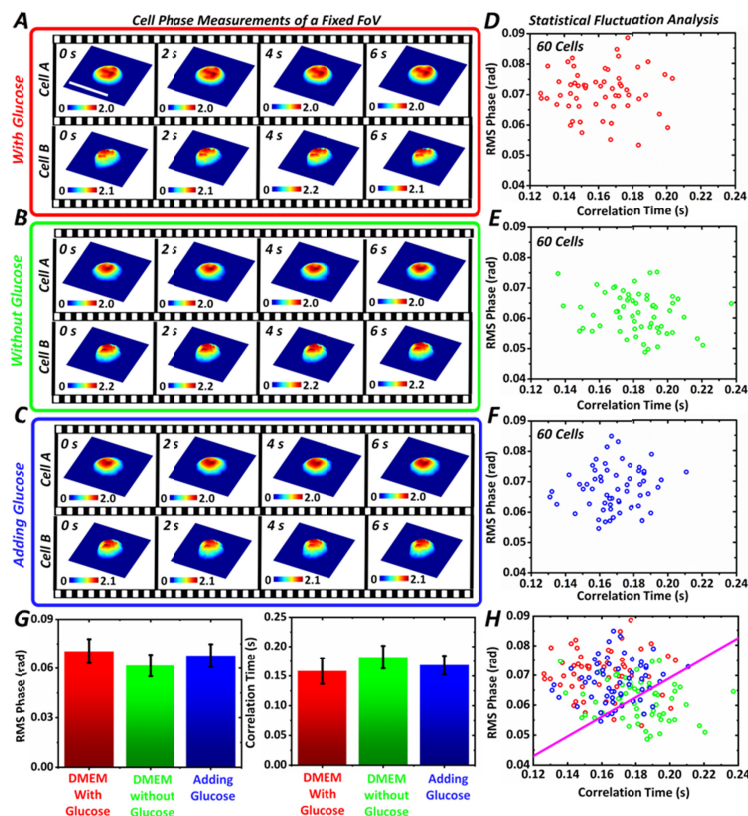


Fig. 6. Cellular fluctuations of F81 cells with ATP and with ATP depletion. (A), (B) and (C) the retrieved phases of 2 representative cells in the DMEM with glucose, in the DMEM without glucose and with glucose adding, respectively. (D), (E) and (F) statistical analysis on the average root-mean-square phase and the correlation time of 60 cells in different conditions corresponding to (A), (B) and (C). (H) Comparisons on statistical root-mean-square phase and correlation time in different conditions. There are statistically significant differences between the root-mean-square phase and the correlation time in (E) and (D/F) ($t < 0.01$), but there are no statistically significant differences between the root-mean-square phase and the correlation time in (D) and (F). (G) Cell condition classification using linear discriminant analysis. The color bars in (A)-(C) indicate the phase with the unit of rad, and the white bar in (A) indicates $30 \mu\text{m}$. The error bars in (H) indicates the standard deviation.

Finally, we have also investigated the cell fluctuations in different ATP concentrations, and the results are shown in Fig. 9. Both F81 cells and BHK21 cells were cultured in DMEM

without glucose but with ATP concentrations of 0 mM , 0.5 mM , 1 mM , 2 mM and 4 mM . Totally 100 cells were measured and 10 cells in each case, and the observation period and the acquisition rate still kept as 6 s and 20 fps , respectively. Figures 9(A) and 9(B) list the retrieved phases of representative F81/BHK21 cells. According to the statistical analysis on root-mean-square phase and correlation time using Student's t test, it is shown that when the ATP concentration was less than 2 mM , the cellular fluctuations increased with higher ATP concentration. While ATP concentration reached 2 mM , there were no much changes in cellular fluctuations even with higher ATP concentration. According to the real-time quantitative phase imaging and cellular fluctuation analysis, it is indicated that ATP can obviously regulate the cellular fluctuations.

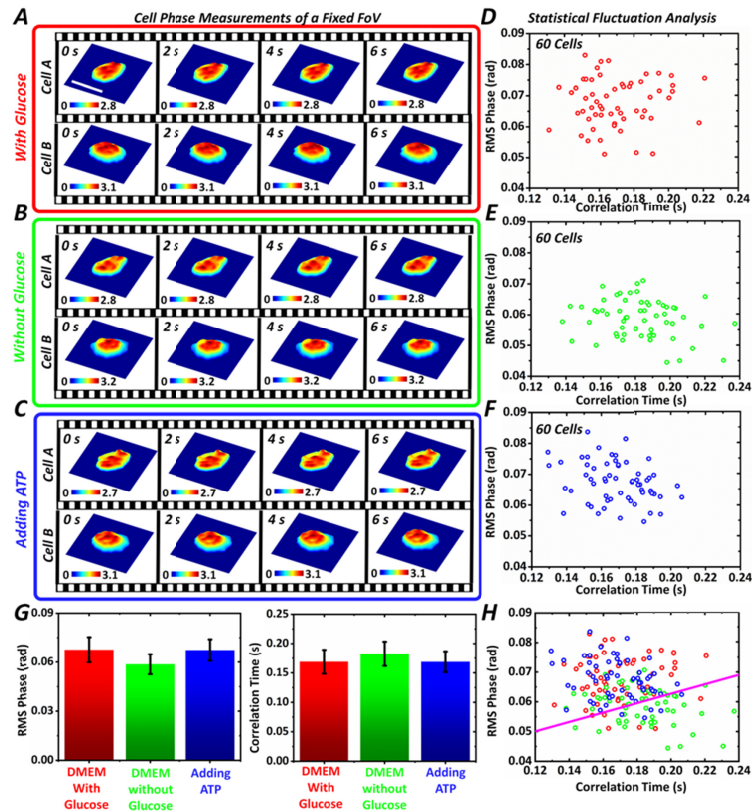


Fig. 7. Cellular fluctuations of BHK21 cells with ATP and with ATP depletion. (A), (B) and (C) the retrieved phases of 2 representative cells in the DMEM with glucose, in the DMEM without glucose and with ATP adding, respectively. (D), (E) and (F) statistical analysis on the average root-mean-square phase and the correlation time of 60 cells in different conditions corresponding to (A), (B) and (C). (H) Comparisons on the statistical root-mean-square phase and correlation time in different conditions. There are statistically significant differences between the root-mean-square phase and the correlation time in (E) and (D/F) ($t < 0.01$), but there are no statistically significant differences between the root-mean-square phase and the correlation time in (D) and (F). (G) Cell condition classification using linear discriminant analysis. The color bars in (A)-(C) indicate the phase with the unit of rad, and the white bar in (A) indicates $30\text{ }\mu\text{m}$. The error bars in (H) indicates the standard deviation.

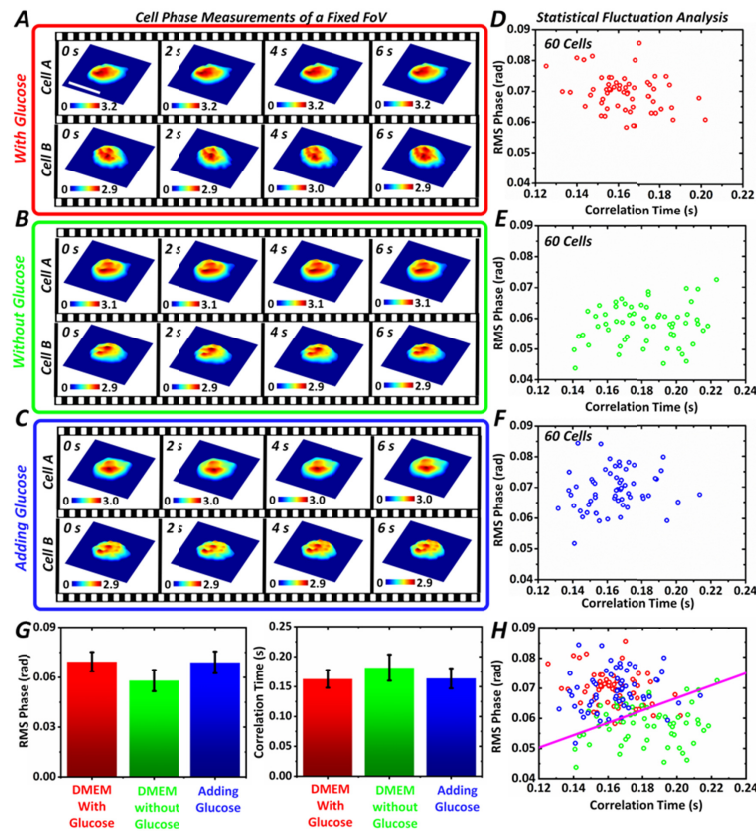


Fig. 8. Cellular fluctuations of BHK21 cells with ATP and with ATP depletion. (A), (B) and (C) the retrieved phases of 2 representative cells in the DMEM with glucose, in the DMEM without glucose and with glucose adding, respectively. (D), (E) and (F) statistical analysis on the average root-mean-square phase and the correlation time of 60 cells in different conditions corresponding to (A), (B) and (C). (H) Comparisons on the statistical root-mean-square phase and correlation time in different conditions. There are statistically significant differences between the root-mean-square phase and the correlation time in (E) and (D/F) ($t < 0.01$), but there are no statistically significant differences between the root-mean-square phase and the correlation time in (D) and (F). (G) Cell condition classification using linear discriminant analysis. The color bars in (A)-(C) indicate the phase with the unit of rad, and the white bar in (A) indicates $30 \mu\text{m}$. The error bars in (H) indicates the standard deviation.

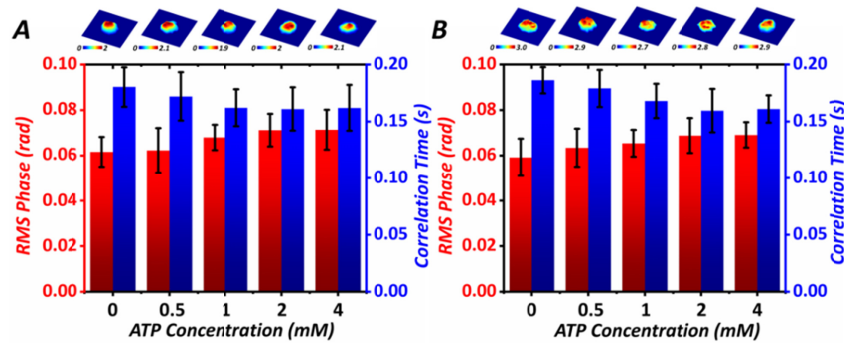


Fig. 9. Relation between the cellular fluctuations and ATP concentrations. Statistical analysis on root-mean-square phase and correlation time of (A) F81 cells and (B) BHK21 cells cultured in DMEM without glucose but with ATP concentrations of 0 mM, 0.5 mM, 1 mM, 2 mM and 4 mM.

3.3 Cellular fluctuation measurements and analysis with AMP-PNP introduction

Figures 10 and 11 show the cellular fluctuations of the F81 and BHK21 cells cultured in the DMEM with glucose, but with AMP-PNP introduction. The observation period and the acquisition rate still kept as 6 s and 20 fps, respectively. Figures 10(A) and 11(A) list the retrieved phases of 4 representative cells from total 120 F81 and BHK21 cells when they were both cultured in the DMEM with glucose. Then, AMP-PNP was introduced into the DMEM, and after 10 min, and the retrieved phases of these 4 cells are shown in Figs. 10(B) and 11(B), respectively. The quantitative analysis on the root-mean-square phase and the correlation time is listed in Figs. 10/11(C) and 10/11(D) corresponding to the conditions of Figs. 10/11(A) and 10/11(B): for F81 cells, the mean root-mean-square phase and the correlation time of 60 different cells are 0.0674 ± 0.0074 rad and 0.1539 ± 0.0173 s before AMP-PNP introduction, however, they become 0.0589 ± 0.0053 rad and 0.1773 ± 0.0189 s after AMP-PNP introduction; and for BHK21 cells, the mean root-mean-square phase and the correlation time of 60 cells are 0.0700 ± 0.0073 rad, 0.1595 ± 0.0165 s before AMP-PNP introduction and 0.0594 ± 0.0061 rad, 0.1886 ± 0.0190 s after AMP-PNP introduction. Figures 10/11(E) shows the statistical comparisons on both the root-mean-square phase and the correlation time. According to Student's t test, there are statistically significant differences between the root-mean-square phase and the correlation time in Figs. 10/11(C) and 10/11(D) ($t < 0.01$). For both the F81 and BHK21 cells, the root-mean-square phase decreased after AMP-PNP introduction indicating that the cellular fluctuation amplitude became lower; and the correlation time increased after AMP-PNP introduction indicating the cellular fluctuation speed became slower. Additionally, linear discriminant analysis was also adopted for analyzing the cell fluctuations before and after AMP-PNP introduction. Figures 10(F) and 11(F) show the classification results, when the cells were cultured with ATP, most of them were distributed upon the line, while after AMP-PNP introduction, most of them were distributed below the line. Therefore, it is proved that when the AMP-PNP as a nonhydrolyzable ATP analog was introduced which competed with ATP to bind to the ATP binding site, both cellular fluctuation amplitude and speed decreased according to the decreased root-mean-square phase and increased correlation time, showing that ATP is a main factor for cellular fluctuations.

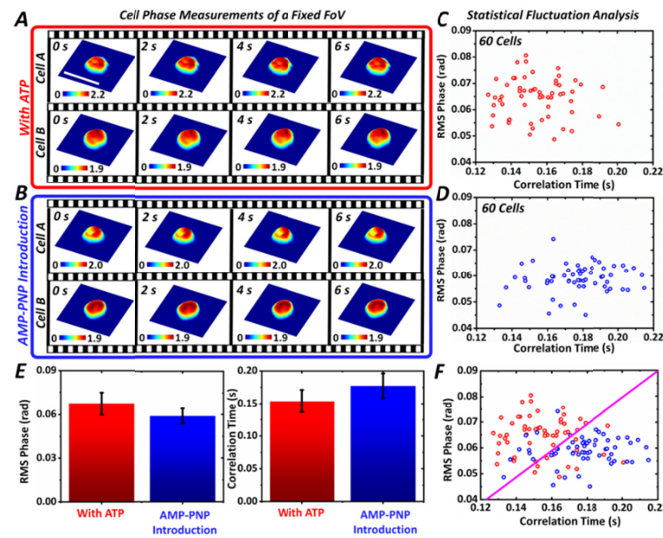


Fig. 10. Cellular fluctuations of F81 cells with AMP-PNP introduction. (A) and (B) the retrieved phases of 2 representative cells in DMEM with glucose and then with AMP-PNP introduction. (C) and (D) statistical analysis on the average root-mean-square phase and the correlation time of 60 cells in different conditions corresponding to (A) and (B). (E) Comparisons on the statistical root-mean-square phase and correlation time in different conditions. There are statistically significant differences between the root-mean-square phase and the correlation time in (C) and (D) ($t < 0.01$). (F) Cell condition classification using linear discriminant analysis. The color bars in (A) and (B) indicate the phase with the unit of rad, and the white bar in (A) indicates $30 \mu\text{m}$. The error bars in (E) indicates the standard deviation.

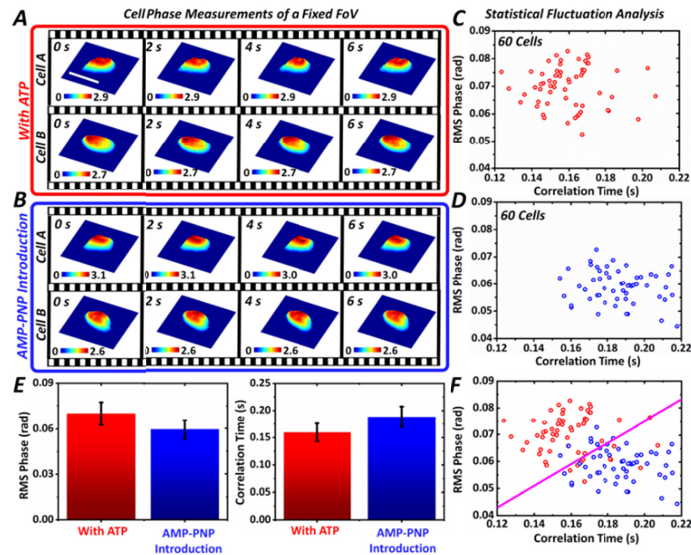


Fig. 11. Cellular fluctuations of BHK21 cells with AMP-PNP introduction. (A) and (B) the retrieved phases of 2 representative cells in DMEM with glucose and then with AMP-PNP introduction. (C) and (D) statistical analysis on the average root-mean-square phase and the correlation time of 60 cells in different conditions corresponding to (A) and (B). (E) Comparisons on the statistical root-mean-square phase and correlation time in different conditions. There are statistically significant differences between the root-mean-square phase and the correlation time in (C) and (D) ($t < 0.01$). (F) Cell condition classification using linear discriminant analysis. The color bars in (A) and (B) indicate the phase with the unit of rad, and the white bar in (A) indicates $30 \mu\text{m}$. The error bars in (E) indicates the standard deviation.

In practical measurements using dual view transport of intensity phase microscopy, real-time phase distributions of both F81 and BHK21 cells in different conditions with ATP and with ATP depletion as well as with AMP-PNP introduction were retrieved. According to quantitative cellular fluctuation analysis, it shows that cellular fluctuation amplitude and speed became increased with higher root-mean-square phase and shorter correlation time in the conditions with ATP than those with ATP depletion or with AMP-PNP introduction, proving that ATP is a factor to regulate cellular mechanics.

4. Conclusion

In order to study the ATP induced cellular fluctuations, real-time cell phase distributions reflecting the cellular fluctuations were retrieved using our proposed dual view transport of intensity phase microscopy. Furthermore, both the root-mean-square phase and the correlation time of cellular fluctuations were computed to quantitatively characterize the cellular fluctuation amplitude and speed, respectively. According to the direct cell phase measurements and the detailed cellular fluctuation analysis, it is found that the cellular fluctuation amplitude and speed of both F81 and BHK21 cells increased in the condition with ATP compared to that with ATP depletion. Besides, when AMP-PNP was introduced which competed with ATP to bind to the ATP binding site, cellular fluctuation amplitude and speed of both cells decreased according to the lower root-mean-square phase and longer correlation time. The result prove that ATP is a factor to regulate cellular mechanics. To our best knowledge, it is the first time that our proposed dual view transport of intensity phase microscopy was successfully used in live cell phase imaging and analysis. The work not only proves that the dual view transport of intensity phase microscopy can provide real-time cell phase imaging for various studies in biological observations and medical diagnostics, but also provides direct measurements on ATP induced cellular fluctuations as a reference to further study on the regulation of ATP on cell mechanics.

Funding

National Key Research and Development Program (2018YFD0500100, 2015BAD12B01); National Natural Science Foundation of China (61705092, 31870154, 31522056, U1730132); Natural Science Foundation of Jiangsu Province of China (BK20170194); Jiangsu Key Research and Development Program (BE2018709); Shanghai Sailing Program (17YF1407000) and Priority Academic Program Development of Jiangsu Higher Education Institutions (PAPD).

Acknowledgements

Authors thank Prof. Keding Yan in Xi'an Technological University for his helps on cellular fluctuation analysis. Authors thank Prof. Huachuan Huang in Southwest University of Science and Technology for his helps on linear discriminant analysis.

Disclosures

The authors declare no competing interests.

References

1. I. Titushkin and M. Cho, "Regulation of Cell Cytoskeleton and Membrane Mechanics by Electric Field: Role of Linker Proteins," *Biophys. J.* **96**(2), 717–728 (2009).
2. J. Lembong, B. Sabass, B. Sun, M. E. Rogers, and H. A. Stone, "Mechanics regulates ATP-stimulated collective calcium response in fibroblast cells," *J. R. Soc. Interface* **12**(108), 20150140 (2015).
3. D. E. Discher, P. Janmey, and Y. L. Wang, "Tissue cells feel and respond to the stiffness of their substrate," *Science* **310**(5751), 1139–1143 (2005).
4. C. M. Lo, H. B. Wang, M. Dembo, and Y. L. Wang, "Cell movement is guided by the rigidity of the substrate," *Biophys. J.* **79**(1), 144–152 (2000).

5. K. Ghosh, Z. Pan, E. Guan, S. Ge, Y. Liu, T. Nakamura, X. D. Ren, M. Rafailovich, and R. A. Clark, "Cell adaptation to a physiologically relevant ECM mimic with different viscoelastic properties," *Biomaterials* **28**(4), 671–679 (2007).
6. A. Banerjee, M. Arha, S. Choudhary, R. S. Ashton, S. R. Bhatia, D. V. Schaffer, and R. S. Kane, "The influence of hydrogel modulus on the proliferation and differentiation of encapsulated neural stem cells," *Biomaterials* **30**(27), 4695–4699 (2009).
7. C. S. Chen, M. Mrksich, S. Huang, G. M. Whitesides, and D. E. Ingber, "Geometric control of cell life and death," *Science* **276**(5317), 1425–1428 (1997).
8. A. J. Engler, S. Sen, H. L. Sweeney, and D. E. Discher, "Matrix elasticity directs stem cell lineage specification," *Cell* **126**(4), 677–689 (2006).
9. M. J. Berridge and R. F. Irvine, "Inositol phosphates and cell signalling," *Nature* **341**(6239), 197–205 (1989).
10. C. D. Ferris, R. L. Haganir, and S. H. Snyder, "Calcium flux mediated by purified inositol 1,4,5-trisphosphate receptor in reconstituted lipid vesicles is allosterically regulated by adenine nucleotides," *Proc. Natl. Acad. Sci. U.S.A.* **87**(6), 2147–2151 (1990).
11. M. J. Sanderson, A. C. Charles, S. Boitano, and E. R. Dirksen, "Mechanisms and function of intercellular calcium signaling," *Mol. Cell. Endocrinol.* **98**(2), 173–187 (1994).
12. S. Tuvia, S. Levin, A. Bitler, and R. Korenstein, "Mechanical fluctuations of the membrane-skeleton are dependent on F-actin ATPase in human erythrocytes," *J. Cell Biol.* **141**(7), 1551–1561 (1998).
13. J. Evans, W. Gratzner, N. Mohandas, K. Parker, and J. Sleep, "Fluctuations of the red blood cell membrane: relation to mechanical properties and lack of ATP dependence," *Biophys. J.* **94**(10), 4134–4144 (2008).
14. T. Betz, M. Lenz, J. F. Joanny, and C. Sykes, "ATP-dependent mechanics of red blood cells," *Proc. Natl. Acad. Sci. U.S.A.* **106**(36), 15320–15325 (2009).
15. Y. Park, C. A. Best, T. Auth, N. S. Gov, S. A. Safran, G. Popescu, S. Suresh, and M. S. Feld, "Metabolic remodeling of the human red blood cell membrane," *Proc. Natl. Acad. Sci. U.S.A.* **107**(4), 1289–1294 (2010).
16. J. Wan, A. M. Forsyth, and H. A. Stone, "Red blood cell dynamics: from cell deformation to ATP release," *Integr. Biol.* **3**(10), 972–981 (2011).
17. Y. Park, C. A. Best, K. Badizadegan, R. R. Dasari, M. S. Feld, T. Kuriabova, M. L. Henle, A. J. Levine, and G. Popescu, "Measurement of red blood cell mechanics during morphological changes," *Proc. Natl. Acad. Sci. U.S.A.* **107**(15), 6731–6736 (2010).
18. Y. Park, M. Diez-Silva, G. Popescu, G. Lykotrafitis, W. Choi, M. S. Feld, and S. Suresh, "Refractive index maps and membrane dynamics of human red blood cells parasitized by *Plasmodium falciparum*," *Proc. Natl. Acad. Sci. U.S.A.* **105**(37), 13730–13735 (2008).
19. H. Byun, T. R. Hillman, J. M. Higgins, M. Diez-Silva, Z. Peng, M. Dao, R. R. Dasari, S. Suresh, and Y. Park, "Optical measurement of biomechanical properties of individual erythrocytes from a sickle cell patient," *Acta Biomater.* **8**(11), 4130–4138 (2012).
20. G. Popescu, L. P. Deflores, J. C. Vaughan, K. Badizadegan, H. Iwai, R. R. Dasari, and M. S. Feld, "Fourier phase microscopy for investigation of biological structures and dynamics," *Opt. Lett.* **29**(21), 2503–2505 (2004).
21. G. Popescu, K. Badizadegan, R. R. Dasari, and M. S. Feld, "Observation of dynamic subdomains in red blood cells," *J. Biomed. Opt.* **11**(4), 040503 (2006).
22. J. Rodenburg and H. Faulkner, "phase retrieval algorithm for shifting illumination," *Appl. Phys. Lett.* **85**(20), 4795–4797 (2004).
23. A. Sun, X. He, Y. Kong, H. Cui, X. Song, L. Xue, S. Wang, and C. Liu, "Ultra-high speed digital micro-mirror device based ptychographic iterative engine method," *Biomed. Opt. Express* **8**(7), 3155–3162 (2017).
24. A. Maiden, D. Johnson, and P. Li, "Further improvements to the ptychographical iterative engine," *Optica* **4**(7), 736–745 (2017).
25. G. Zheng, R. Horstmeyer, and C. Yang, "Wide-field, high-resolution Fourier ptychographic microscopy," *Nat. Photonics* **7**(9), 739–745 (2013).
26. G. Zheng, "Breakthroughs in Photonics 2013: Fourier Ptychographic Imaging," *IEEE Photonics J.* **6**(2), 0701207 (2014).
27. R. Eckert, Z. F. Phillips, and L. Waller, "Efficient illumination angle self-calibration in Fourier ptychography," *Appl. Opt.* **57**(19), 5434–5442 (2018).
28. A. Greenbaum, W. Luo, T. W. Su, Z. Göröcs, L. Xue, S. O. Isikman, A. F. Coskun, O. Mudanyali, and A. Ozcan, "Imaging without lenses: achievements and remaining challenges of wide-field on-chip microscopy," *Nat. Methods* **9**(9), 889–895 (2012).
29. M. M. Villone, P. Memmolo, F. Merola, M. Mugnano, L. Miccio, P. L. Maffettone, and P. Ferraro, "Full-angle tomographic phase microscopy of flowing quasi-spherical cells," *Lab Chip* **18**(1), 126–131 (2018).
30. T. Cacace, V. Bianco, M. Paturzo, P. Memmolo, M. Vassalli, M. Fraldi, G. Mensitieri, and P. Ferraro, "Retrieving acoustic energy densities and local pressure amplitudes in microfluidics by holographic time-lapse imaging," *Lab Chip* **18**(13), 1921–1927 (2018).
31. Z. Jiang, X. Pan, Y. Kong, W. Qian, S. Wang, and C. Liu, "Partial saturation-aided resolution enhancement for digital holography," *Appl. Opt.* **57**(14), 3884–3889 (2018).
32. B. Tayebi, J. H. Han, F. Sharif, M. R. Jafarfar, and D. Y. Kim, "Compact single-shot four-wavelength quantitative phase microscopy with polarization- and frequency-division demultiplexing," *Opt. Express* **25**(17), 20172–20182 (2017).

33. C. Hu, S. Zhu, L. Gao, and G. Popescu, "Endoscopic diffraction phase microscopy," *Opt. Lett.* **43**(14), 3373–3376 (2018).
34. M. Shan, M. E. Kandel, and G. Popescu, "Refractive index variance of cells and tissues measured by quantitative phase imaging," *Opt. Express* **25**(2), 1573–1581 (2017).
35. K. Kim, W. S. Park, S. Na, S. Kim, T. Kim, W. Do Heo, and Y. Park, "Correlative three-dimensional fluorescence and refractive index tomography: bridging the gap between molecular specificity and quantitative bioimaging," *Biomed. Opt. Express* **8**(12), 5688–5697 (2017).
36. K. Kim and Y. Park, "Tomographic active optical trapping of arbitrarily shaped objects by exploiting 3D refractive index maps," *Nat. Commun.* **8**, 15340 (2017).
37. W. Choi, C. Fang-Yen, K. Badizadegan, S. Oh, N. Lue, R. R. Dasari, and M. S. Feld, "Tomographic phase microscopy," *Nat. Methods* **4**(9), 717–719 (2007).
38. L. Wolbromsky, N. A. Turko, and N. T. Shaked, "Single-exposure full-field multi-depth imaging using low-coherence holographic multiplexing," *Opt. Lett.* **43**(9), 2046–2049 (2018).
39. A. Nativ and N. T. Shaked, "Compact interferometric module for full-field interferometric phase microscopy with low spatial coherence illumination," *Opt. Lett.* **42**(8), 1492–1495 (2017).
40. K. Yan, L. Xue, and S. Wang, "Field of view scanning based quantitative interferometric microscopic cytometers for cellular imaging and analysis," *Microsc. Res. Tech.* **81**(4), 397–407 (2018).
41. A. Shanker, L. Tian, M. Sczyrba, B. Connolly, A. Neureuther, and L. Waller, "Transport of intensity phase imaging in the presence of curl effects induced by strongly absorbing photomasks," *Appl. Opt.* **53**(34), J1–J6 (2014).
42. X. Meng, H. Huang, K. Yan, X. Tian, W. Yu, H. Cui, Y. Kong, L. Xue, C. Liu, and S. Wang, "Smartphone based hand-held quantitative phase microscope using the transport of intensity equation method," *Lab Chip* **17**(1), 104–109 (2017).
43. J. Hu, Y. Kong, Z. Jiang, L. Xue, F. Liu, C. Liu, and S. Wang, "Adaptive dual-exposure fusion-based transport of intensity phase microscopy," *Appl. Opt.* **57**(25), 7249–7258 (2018).
44. L. Tian, J. C. Petrucci, and G. Barbastathis, "Nonlinear diffusion regularization for transport of intensity phase imaging," *Opt. Lett.* **37**(19), 4131–4133 (2012).
45. L. Tian, J. C. Petrucci, Q. Miao, H. Kudrolli, V. Nagarkar, and G. Barbastathis, "Compressive x-ray phase tomography based on the transport of intensity equation," *Opt. Lett.* **38**(17), 3418–3421 (2013).
46. L. Waller, S. S. Kou, C. J. Sheppard, and G. Barbastathis, "Phase from chromatic aberrations," *Opt. Express* **18**(22), 22817–22825 (2010).
47. L. Waller, Y. Luo, S. Y. Yang, and G. Barbastathis, "Transport of intensity phase imaging in a volume holographic microscope," *Opt. Lett.* **35**(17), 2961–2963 (2010).
48. Z. Yang and Q. Zhan, "Single-Shot Smartphone-Based Quantitative Phase Imaging Using a Distorted Grating," *PLoS One* **11**(7), e0159596 (2016).
49. W. Yu, X. Tian, X. He, X. Song, L. Xue, C. Liu, and S. Wang, "Real time quantitative phase microscopy based on single-shot transport of intensity equation (ssTIE) method," *Appl. Phys. Lett.* **109**(7), 071112 (2016).
50. Y. Li, J. Di, C. Ma, J. Zhang, J. Zhong, K. Wang, T. Xi, and J. Zhao, "Quantitative phase microscopy for cellular dynamics based on transport of intensity equation," *Opt. Express* **26**(1), 586–593 (2018).
51. C. Zuo, Q. Chen, W. Qu, and A. Asundi, "Noninterferometric single-shot quantitative phase microscopy," *Opt. Lett.* **38**(18), 3538–3541 (2013).
52. X. Tian, W. Yu, X. Meng, A. Sun, L. Xue, C. Liu, and S. Wang, "Real-time quantitative phase imaging based on transport of intensity equation with dual simultaneously recorded field of view," *Opt. Lett.* **41**(7), 1427–1430 (2016).
53. Q. Gong, Q. Wei, J. Xu, Y. Kong, Z. Jiang, W. Qian, Y. Zhu, L. Xue, F. Liu, C. Liu, and S. Wang, "Digital field of view correction combined dual-view transport of intensity equation method for real time quantitative imaging," *Opt. Eng.* **57**(06), 063102 (2018).
54. P. Memmolo, C. Distanto, M. Paturzo, A. Finizio, P. Ferraro, and B. Javidi, "Automatic focusing in digital holography and its application to stretched holograms," *Opt. Lett.* **36**(10), 1945–1947 (2011).
55. J. Xu, X. Tian, X. Meng, Y. Kong, S. Gao, H. Cui, F. Liu, L. Xue, C. Liu, and S. Wang, "Wavefront-sensing-based autofocusing in microscopy," *J. Biomed. Opt.* **22**(8), 1–7 (2017).
56. S. Wang, L. Xue, and K. Yan, "Numerical calculation of light scattering from metal and dielectric randomly rough Gaussian surfaces using microfacet slope probability density function based method," *J. Quant. Spectrosc. Radiat. Transf.* **196**, 183–200 (2017).
57. L. Ma, G. Rajshekhar, R. Wang, B. Bhaduri, S. Sridharan, M. Mir, A. Chakraborty, R. Iyer, S. Prasanth, L. Millet, M. U. Gillette, and G. Popescu, "Phase correlation imaging of unlabeled cell dynamics," *Sci. Rep.* **6**(1), 32702 (2016).
58. M. Soto and E. Acosta, "Improved phase imaging from intensity measurements in multiple planes," *Appl. Opt.* **46**(33), 7978–7981 (2007).
59. A. M. Zysk, R. W. Schoonover, P. S. Carney, and M. A. Anastasio, "Transport of intensity and spectrum for partially coherent fields," *Opt. Lett.* **35**(13), 2239–2241 (2010).
60. L. Waller, L. Tian, and G. Barbastathis, "Transport of Intensity phase-amplitude imaging with higher order intensity derivatives," *Opt. Express* **18**(12), 12552–12561 (2010).
61. B. Xue, S. Zheng, L. Cui, X. Bai, and F. Zhou, "Transport of intensity phase imaging from multiple intensities measured in unequally-spaced planes," *Opt. Express* **19**(21), 20244–20250 (2011).

62. Z. Jingshan, R. A. Claus, J. Dauwels, L. Tian, and L. Waller, "Transport of Intensity phase imaging by intensity spectrum fitting of exponentially spaced defocus planes," *Opt. Express* **22**(9), 10661–10674 (2014).
63. Y. Eguchi, S. Shimizu, and Y. Tsujimoto, "Intracellular ATP levels determine cell death fate by apoptosis or necrosis," *Cancer Res.* **57**(10), 1835–1840 (1997).
64. J. Shao, Y. Wang, X. Deng, and S. Wang, "Sparse linear discriminant analysis by thresholding for high dimensional data," *Ann. Stat.* **39**(2), 1241–1265 (2011).